COMMUNICATION

Check for updates

Molybdenum *in situ* etching-treated ultrathin NiFeMo LDHs nanosheet arrays as a performance anodic catalyst for efficient industrial production of hydrogen†

Zhiqun Bai,[a] Ruoxuan Guo,[a] Jingwang Kuang,[a] Huifang Chen,[a] WeiHao Sha,[a] Ao Xie,[a] Jingchao Liu, [ID] *[b] Pingyu Wan[a] and Yang Tang*[a]

Water-splitting is a critical technology for the conversion and storage of renewable energy. The slow anodic process dynamics with high overpotential greatly limit the commercialization of electrolytic hydrogen production. Herein, we proposed an electrochemical *in situ* etching method to achieve molybdenum component-controlled dissolution of ultrathin NiFeMo layered double hydroxides (LDHs) nanosheet arrays on nickel–iron foam (NFF) to create *in situ* reconstructed oxygen evolution reaction (OER) active sites in LDHs. The Mo-etched material exhibited significantly enhanced catalytic performance and demonstrated exceptional OER activity in alkaline media, achieving a low overpotential of 288 mV at 10 mA cm^{-2} and 784 mV at 1000 mA cm^{-2}, along with a desired Tafel slope of 43.52 mV dec^{-1}. The enhanced reaction kinetics was contributed by Mo doping-induced electronic structure optimization and interfacial stabilization. Furthermore, an assembled alkaline electrolyzer with NiFeMo/NFF maintained a stable electrolysis voltage (1.695 ± 0.022 V) under simulated industrial fluctuating conditions (30 wt% KOH, 85 °C, 3000 A m^{-2}) for 210 h, exhibiting a super-low voltage decay rate (0.1 mV h^{-1}). The superior performance-stability properties of the new catalyst displayed new material design strategies for efficient industrial hydrogen-production systems.

1 Introduction

The rapid increase in global energy demand driven by population growth and economic development has accelerated the transition towards renewable energy technologies.[1] Global energy demand is increasing year-by-year. At present, the main energy resources are crude oil, natural gas and coal, but they are not renewable and are harmful to the environment.[2] Hydrogen, as a carbon-neutral and storable energy carrier, has emerged as a pivotal solution for carbon neutrality.[3] However, the efficiency of renewable energy utilization *via* water electrolysis is severely limited by the high overpotential of the oxygen evolution reaction (OER) and the prohibitive cost of precious metal catalysts (*e.g.*, IrO$_2$).[4] Thus, developing low-cost,[5] highly active, and stable non-precious OER electrocatalysts has become a critical scientific challenge.

Nickel–iron (NiFe)-based transition metal oxides/hydroxides have garnered significant attention due to their abundance and cost-effectiveness. In 2014, Lu and colleagues found that nickel–iron LDH nanosheet arrays exhibited excellent catalytic activity and stability against the OER. NiFe LDH nanosheet arrays were prepared on three-dimensional nickel foam substrates after hydrothermal treatment at 120 °C for 12 h. This strategy could provide abundant active sites, promote gas precipitation, and have small charge transfer resistance, which is conducive to the electron transfer process.[6] Studies have shown that activity can be significantly improved by elemental doping (*e.g.*, Mo, Co), defect engineering or nanostructuring. Ding Lei *et al.* used a simple and rapid one-step electrodeposition process to prepare W-doped NiFe (NiFeW)-layered dihydroxide with ultrathin nanosheet characteristics at room temperature and pressure as a bifunctional catalyst for water electrolysis.[7] Chen and colleagues prepared a FeCo$_2$O$_4$/MoS$_2$ binary composite catalyst by a hydrothermal method and calcination method. It was found that MoS$_2$ had high activity and good stability in the HER, and was more promising than precious metal catalysts. In oxidative dynamics, its rich redox potential enabled it to adsorb ions (Co^{2+}/Co^{3+}, Fe^{2+}/Fe^{3+}) and enhance the activity of the OER.[8] Doping (*e.g.*, Mo, Co), defect engineering, and nanostructuring have enhanced their activity,[9] but two fundamental issues remain unresolved: (1) insufficient active site density leading to high overpotentials; (2) structural degradation (peeling/oxidation) under harsh operational conditions (*e.g.*, elevated temperature/current density).[10] Although third-metal incorporation can optimize

[a]Institute of Electrochemistry, Beijing University of Chemical Technology, Beijing 100029, China
[b]School of Computer Science and Engineering, Beihang University, Beijing 100191, China. E-mail: liujingchao@buaa.edu.cn

† Electronic supplementary information (ESI) available. See DOI: https://doi.org/10.1039/d5nr01666e

electronic structures for activity, conventional chemical doping often causes segregation of active species[11] and fails to address interfacial stability. In addition, the lack of precise control of nanomorphology in wet chemical synthesis limits the further improvement of performance. Hence, we used an electrochemical deposition method to synthesize Mo-doped stable catalysts more conveniently.

We developed a highly efficient and stable NiFeMo/NFF electrocatalyst, which exhibited OER performance in alkaline media. Electrochemical measurements revealed that the NiFeMo/NFF catalyst achieved an overpotential of 288 mV at 10 mA cm^{-2} and 784 mV at 1000 mA cm^{-2} in 1 M KOH electrolyte, demonstrating superior electrocatalytic activity. Kinetic analyses further confirmed its optimized reaction kinetics, as evidenced by a Tafel slope of 43.52 mV dec^{-1}. To evaluate practical applicability, a prototype alkaline electrolyzer assembled with NiFeMo/NFF was subjected to simulated industrial fluctuating conditions (30 wt% KOH electrolyte, 85 °C, and 3000 A m^{-2}) for 210 h of continuous operation, during which the electrolysis voltage remained stable at 1.695 ± 0.022 V with a negligible voltage decay rate of 0.1 mV h^{-1}, showcasing exceptional dynamic response capability and long-term durability. The synergistic enhancement in performance and stability originated from dual mechanisms: Mo doping-induced optimization of electronic structure and interfacial stabilization. These mechanisms provide new material design strategies for developing highly active and durable OER catalysts "tailored" for industrial hydrogen-production systems.

2 Experimental section

2.1 Materials

All chemicals used in this study were of analytical purity. Ferrous sulfate (FeSO$_4$) and sodium molybdate dihydrate (Na$_2$MoO$_4$·2H$_2$O) were purchased from Aladdin Reagents Co., Ltd. Ammonium sulfate ((NH$_4$)$_2$SO$_4$) and sodium chloride (NaCl) were supplied by Fuchen Chemical Reagents Co., Ltd. Sodium nitrate (NaNO$_3$), hydrochloric acid (HCl), ethanol (C$_2$H$_5$OH), and potassium hydroxide (KOH) were obtained from Beijing Chemical Reagents Co., Ltd. The 50% nickel–iron foam (NFF) substrate used in this work was provided by Lizhiyuan Battery Co., Ltd.

2.2 Synthesis of materials

2.2.1 Pretreatment of NFF. Nickel–iron foam (NFF) substrates (1 cm × 1 cm) were sequentially ultrasonically cleaned in ethanol, hydrochloric acid, and ultrapure water for 15 min each, followed by drying at ambient temperature for subsequent experiments.

2.2.2 Synthesis of NiFeMo/NFF. Pre-treated NFF was employed as the working electrode, while a titanium ruthenium iridium (TiRuIr) electrode served as the counter electrode. Electrochemical etching was performed in a 50 mL mixed solution containing 30 mM sodium molybdate (Na$_2$MoO$_4$) and 15 mM sodium chloride (NaCl). The etching

process consisted of two stages. The first stage was a positive current density of 30 mA cm^{-2} applied for 120 s. The second stage was a negative current density of −30 mA cm^{-2} maintained for 20 s.

This two-stage cycle was repeated 20 times to complete the etching process, yielding electrode A. Subsequently, electrode A was rinsed with ultrapure water and dried in a vacuum oven at 70 °C. After drying, electrode A was thermally annealed in a muffle furnace to obtain the final NiFeMo/NFF composite electrode.

2.3 Material characterization

A combination of advanced characterization techniques was employed to investigate the structure and composition of NiFeMo/NFF. Scanning electron microscopy (SEM; AFM5500) was used to examine the morphology and microstructure, while energy-dispersive X-ray spectroscopy (EDS) provided elemental distribution maps. X-ray diffraction (XRD; Ultima III) was utilized to analyze crystal structure and phase composition. High-resolution transmission electron microscopy (HRTEM; Talos F200S; FEI) was employed to observe lattice fringes at nanoscale resolution, enabling precise determination of crystallographic planes. Raman spectroscopy (Renishaw inVia Reflex Raman spectroscope) with a 785 nm laser excitation wavelength was used to probe the fine structural features. Finally, X-ray photoelectron spectroscopy (XPS; K-Alpha; Thermo Scientific) was applied to analyze the surface elemental composition and chemical states. These multi-scale characterization methods collectively revealed the hierarchical structural and compositional characteristics of NiFeMo/NFF, providing a scientific basis for its electrocatalytic performance.

2.4 Electrochemical measurements

All electrochemical measurements were conducted at room temperature using a CS 150 M electrochemical workstation manufactured by Wuhan Kestech Instruments Co., Ltd. The three-electrode system consisted of the prepared NiFeMo/NFF electrode (1 cm × 1 cm) as the working electrode, a titanium ruthenium (TiRu) electrode as the counter electrode (CE), and a saturated calomel electrode (SCE) as the reference electrode (RE). The potential was referenced to the reversible hydrogen electrode (RHE) using the equation: E vs. RHE = E vs. SCE + 0.2415 + 0.059 × pH. The electrolyte used was 1 M KOH solution.

For comparative analyses, the electrochemical performance of NiFeMo/NFF, NiFe/NFF, and NFF electrodes was evaluated. Linear sweep voltammetry (LSV) was employed to measure the relationship between overpotential and current density, with the voltage scan range set from 0 to 1 V at a scan rate of 5 mV s^{-1}. The Tafel slope was calculated using the equation $\eta = a + b \log J$, where η is the overpotential, b is the Tafel slope, and J is the current density. Chronoamperometry was performed at various current densities (10, 100, 300, 500, 800, and 1000 mA cm^{-2}) to monitor the potential decay over time. Cyclic voltammetry (CV) was conducted in the non-faradaic region with scan rates ranging from 10 to 100 mV s^{-1}. The double-layer capaci-

tance (C_{dl}) was determined by fitting the CV curves, and the effective electrode surface area (ECSA) was calculated using the formula ECSA = A C_{dl}/C_s, where A = 1 cm² (electrode area) and C_s = 0.04 mF cm⁻² (standard value for ECSA determination).

Finally, electrochemical impedance spectroscopy (EIS) was performed in potentiostatic mode at a constant current density of 10 mA cm⁻², with frequency ranging from 105 Hz to 10⁻² Hz and an alternating signal amplitude of 3 mV. Long-term stability testing under industrial alkaline electrolysis conditions was carried out using a Blue & Battery test system (D350A) to evaluate the durability of the electrode in real-world applications.

3 Results and discussion

3.1 Structural analyses

Nickel–iron foam (NFF) was selected as the catalyst support due to its porous network structure, high electrical conductivity, and dual functionality as both Ni and Fe sources during catalysis. The NiFeMo/NFF electrode was synthesized as shown in Fig. 1. During the electrochemical reaction, Cl⁻ etched the NFF to release N²⁺ and Fe³⁺, while OH⁻ generated during reduction combined with MoO_4^{2-} to deposit on the electrode surface. Simple thermal annealing removed residual crystallization water and enhanced crystallinity, yielding the final NiFeMo/NFF composite.

As shown in Fig. 2a–c, the Mo-doped NiFeMo/NFF electrode exhibited aggregated nanoparticle structures (~486.9 nm, as observed in Fig. S1†), indicating a large specific surface area and abundant electrochemical active sites. Notably, Mo doping acted as an effective corrosion inhibitor: the undoped NiFe/NFF electrode exhibited severe surface cracking (Fig. 2d–f), whereas the NiFeMo/NFF electrode maintained a uniform and intact surface morphology. This structural integrity contributed directly to enhanced catalytic activity and long-term stability.

The corresponding energy-dispersive X-ray (EDS) mapping confirmed uniform elemental distribution of Ni, Fe, Mo, and O across the NiFeMo/NFF electrode (Fig. 2g). The atomic percentage was quantified as Ni (22.06%), Fe (19.72%), Mo (2.99%), and O (53.32%) (Table S1†).

X-ray diffraction (XRD) analyses (Fig. S2†) indicated that the NiFeMo/NFF composite material exhibited typical Ni crystal
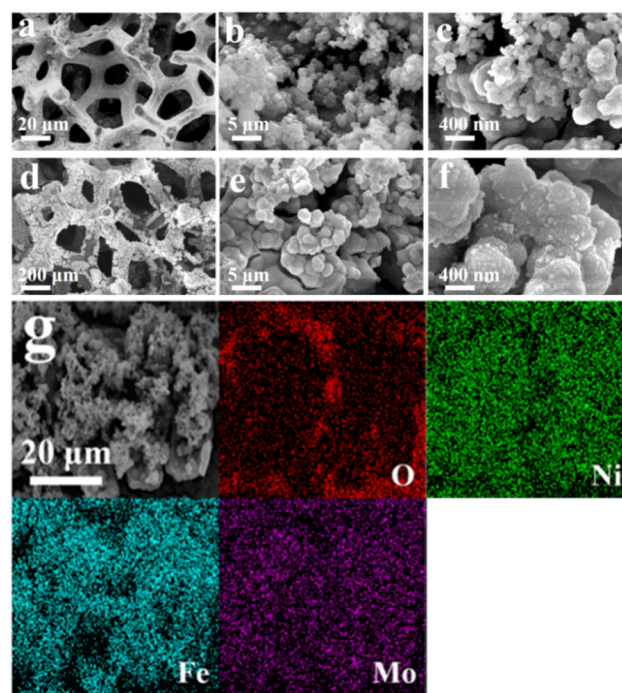

Fig. 2 (a–c) SEM images of NiFeMo/NFF showing a nanoporous framework and hierarchical porosity. (d–f) SEM images of NiFe/NFF exhibiting a flatter surface morphology. (g) EDS elemental mapping of NiFeMo/NFF.

structure characteristics. The diffraction peaks observed at 44.5°, 51.85°, and 76.4° perfectly matched the (111), (200), and (220) crystal planes of standard Ni (PDF#: 04-0850). Notably, the XRD spectrum of NiFeMo/NFF did not show significant differences compared with NiFe/NFF, which may have been due to the strong diffraction signal from the substrate material masking other possible crystal phase features, such as NiFe-LDH and NiFe₂O₄. Subsequent high-resolution transmission electron microscopy (HRTEM) further confirmed the microstructure and revealed the presence of localized crystallization regions.

HRTEM of the morphology and lattice fringes of the electrode material is presented in Fig. 3. Initial observations of the surface morphology revealed that wrinkled nanosheets formed a "nanoflower"-like structure. Lattice fringe measurements
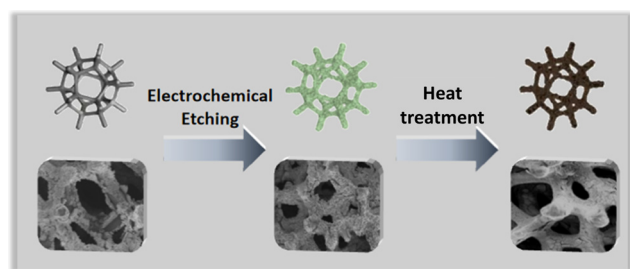

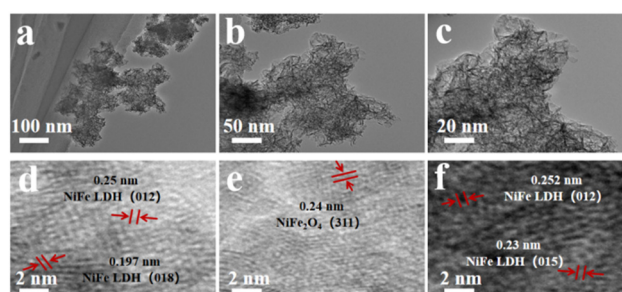**Fig. 1** Mo-doped NiFeMo/NFF electrode prepared *via* hydrothermal synthesis.

Fig. 3 (a–f) HRTEM images of NiFeMo/NFF.

identified spacings of 0.197 nm, 0.23 nm, 0.25 nm, and 0.24 nm, corresponding to the (018), (015), (012) crystal planes of NiFe-LDH and the (311) crystal plane of $NiFe_2O_4$, respectively. These data further confirmed the presence of both NiFe-LDH and $NiFe_2O_4$ components on the surface, indicating that the nanosheets were composed of NiFe oxides and NiFe-LDH. The strong diffraction peaks from the NFF substrate may have overshadowed other component peaks. Additionally, the poor crystallinity of NiFeMo/NFF (predominantly amorphous structure) likely explained the absence of distinct Mo elemental peaks in the XRD pattern.

X-ray photoelectron spectroscopy (XPS) was employed to investigate the chemical composition and electronic states of NiFeMo/NFF and NiFe/NFF, as shown in Fig. 4a–e. The NiFe/NFF surface consisted primarily of Ni, Fe, and O elements, while the NiFeMo/NFF spectrum confirmed the coexistence of Ni, Fe, Mo, and O, consistent with EDS results, thereby verifying Mo doping.

As depicted in Fig. 4b, the high-resolution Ni 2p XPS spectrum of NiFeMo/NFF exhibited peaks at 855.43 eV and 873.25 eV, corresponding to the Ni^{2+} $2p_{3/2}$ and $2p_{1/2}$ transitions, respectively. Additional peaks at 856.90 eV and 875.06 eV were attributed to Ni^{3+} 2p orbital splitting. Notably, satellite peaks characteristic of Ni–O bonds were observed at 862.03 eV and 880.25 eV. Quantitative peak fitting revealed that the area of the Ni^{3+} $2p_{3/2}$ peak in the Mo-doped catalyst was 121.5% greater than that of the undoped sample, indicating that Mo^{6+} modified the electronic structure of Ni^{2+} through electron transfer and d-orbital coupling, rendering it more prone to lose electrons and oxidize into Ni^{3+}. Moreover, the crystal-field distortion induced by Mo^{6+} enhanced the asymmetry of the local coordination field, optimizing the oxidation potential energy of Ni^{2+}. Meanwhile, it could further facilitate the conversion of Ni^{2+} to Ni^{3+} by modulating oxygen activity or adsorp-

tion behavior, ultimately increasing the Ni^{3+} content significantly.

Further analyses suggested that Mo doping modulated the local electronic structure of Ni sites, enhancing the electron-capture capability of adjacent O atoms and thereby optimizing the charge transfer efficiency. This mechanism enabled Ni^{2+} to lose electrons readily and form high-valent Ni^{3+} species, which are crucial for efficient OER catalysis.

Fig. 4c presents the high-resolution Fe 2p XPS spectrum of NiFeMo/NFF. The peaks at 711.04 eV and 724.05 eV corresponded to Fe^{2+} $2p_{3/2}$ and $2p_{1/2}$ orbitals, respectively. Meanwhile, peaks at 713.53 eV and 725.91 eV were attributed to Fe^{3+} 2p orbital transitions. Notably, Mo doping induced a leftward shift in the Fe^{2+} $2p_{3/2}$ binding energy by 0.31 eV and the Fe^{3+} $2p_{3/2}$ peak by 0.25 eV. This chemical-shift phenomenon indicated that Mo altered the local electronic environment of Fe atoms significantly, potentially through electronic interactions or coordination restructuring between Mo and Fe (e.g., Mo acting as an electron donor/acceptor). Additionally, the satellite peaks observed at 718.06 eV and 731.75 eV further confirmed the complex chemical states of Fe, suggesting non-crystalline matrix environments and possible surface oxidation effects. The $3d^6$ configuration of Fe^{2+} inherently exhibited high oxidation inertia in strongly alkaline environments (compared with Ni^{2+}), and the electron cloud distribution of its d orbitals showed a weak response to electron transfer from Mo^{6+}. As shown in Fig. 4c, although the Fe^{2+} 2p peak shifted leftwards, the proportion of Fe^{3+} did not increase significantly, indicating that the electron transfer failed to drive the oxidation of Fe^{2+} to Fe^{3+}.[12,13]

Fig. 4d shows the high-resolution O 1s XPS spectrum, revealing significant contributions from multiple oxygen species. Peak-fitting analysis identified two primary components: 529.94 eV (lattice oxygen bound to metal centers,
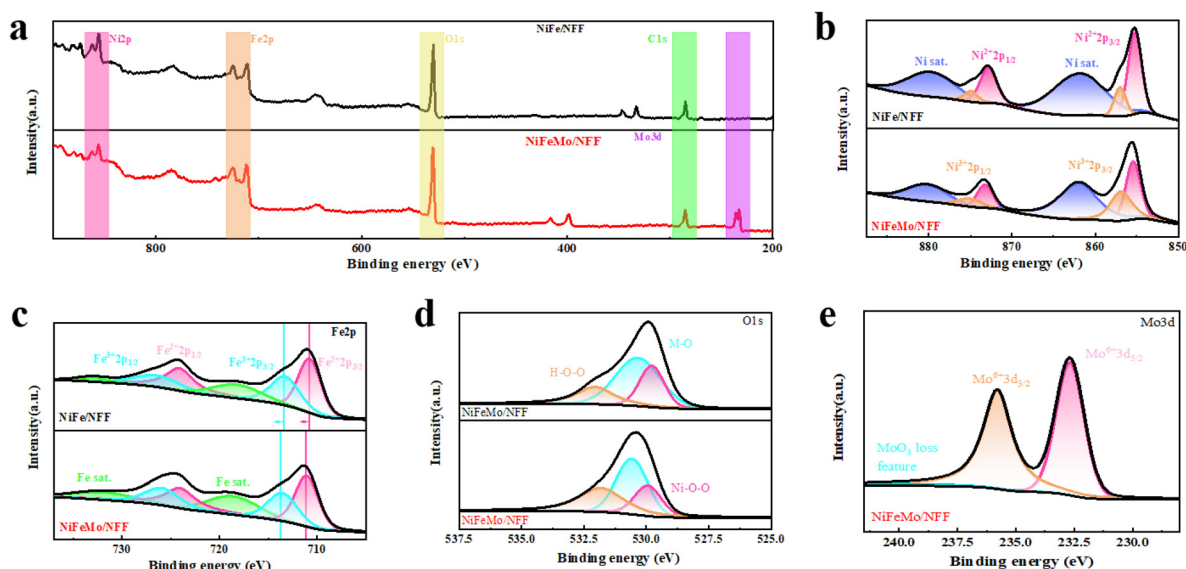

Fig. 4 (a) XPS wide spectrum of NiFe/NFF and NiFeMo/NFF. (b) Deconvolved Ni 2p, (c) Fe 2p, (d) O 1s, and (e) Mo 3d peak-fitting spectra.

M–O) and 530.58 eV (stable coordination structures). Notably, a shoulder peak at 531.82 eV was attributed to surface hydroxyl oxygen species (O–H) or chemisorbed oxygen near defect sites, directly linked to the presence of surface oxygen vacancies. Quantitative analyses revealed that the area of the O–H–H related shoulder peak in Mo-doped samples increased by 115.6% compared with the undoped counterpart, confirming that transition metal doping effectively promoted the formation of surface hydroxyl oxide active phases.

Based on the high-resolution analysis of Mo 3d XPS (Fig. 4e), incorporation of high-valent Mo (Mo^{6+}) into the catalyst system was confirmed. Peak fitting revealed that the characteristic peaks at 232.68 eV (Mo $3d_{5/2}$) and 235.79 eV (Mo $3d_{3/2}$) corresponded to the typical binding energies of Mo^{6+}, indicating that Mo existed stably in the +6 oxidation state within the composite.

Introduction of this high-valent dopant induced significant reconstruction of electronic structure, demonstrating that Mo doping redistributed the electron density at Ni/Fe sites and promoted the transformation of Ni^{2+} to highly active Ni^{3+} species. Combined with O 1s spectrum analysis, the strong electronegativity of Mo^{6+} optimized the coordination environment of metal centers, but also enhanced the activation of lattice oxygen through the Jahn–Teller effect, thereby further improving catalytic performance.

3.2 Electrochemical performance

A standard three-electrode system was employed to systematically evaluate the OER performance of NFF, NiFe/NFF, and NiFeMo/NFF catalysts in 1 M KOH electrolyte. Fig. 5a–f presents the LSV curves before IR compensation, revealing that NiFeMo/NFF exhibited significantly enhanced electrocatalytic activity compared with NFF and NiFe/NFF. To probe the reaction kinetics, Tafel slopes were derived from the LSV curves (Fig. 5b). The NiFeMo/NFF catalyst exhibited a Tafel slope of 43.52 mV dec^{-1}, which was significantly lower than those of NFF and NiFe/NFF, indicating its superior charge transfer efficiency and optimized reaction kinetics—direct evidence of the intrinsic activation effect of Mo doping.

To assess OER performance quantitatively, Fig. 5c summarizes the overpotentials (η_{10} and η_{1000}) at current densities of 10 and 1000 mA cm^{-2} (without IR compensation). As shown in Table S2,† NiFeMo/NFF demonstrated the lowest overpotentials across all current densities: η_{10} = 288 mV and η_{1000} = 784 mV. Post-IR compensation (65%), the LSV curves (Fig. S3†) revealed further improvements (η_{100} = 322 mV and η_{1000} = 331 mV), confirming its exceptional electrocatalytic activity under industrial-relevant conditions.

Systematic evaluation of OER performance was further conducted via chronoamperometry. Fig. 5d shows the current–time responses at stepwise current densities (10–1000 mA cm^{-2}, each maintained for 300 s). All samples exhibited structural stability, with NiFeMo/NFF demonstrating the most pronounced OER activity, characterized by the lowest polarization curve. This result highlighted the synergistic effect of Mo doping in simultaneously enhancing both activity and durability.

Fig. 5e shows the double-layer capacitance fitting curves of four materials. The NiFeMo/NFF material exhibited the highest double-layer capacitance at 14.28 mF cm^{-2}, significantly surpassing that of NiFe/NFF (C_{dl} = 3.36 mF cm^{-2}) and NFF (0.94 mF cm^{-2}) by 4.25-times and 15.19-times, respect-
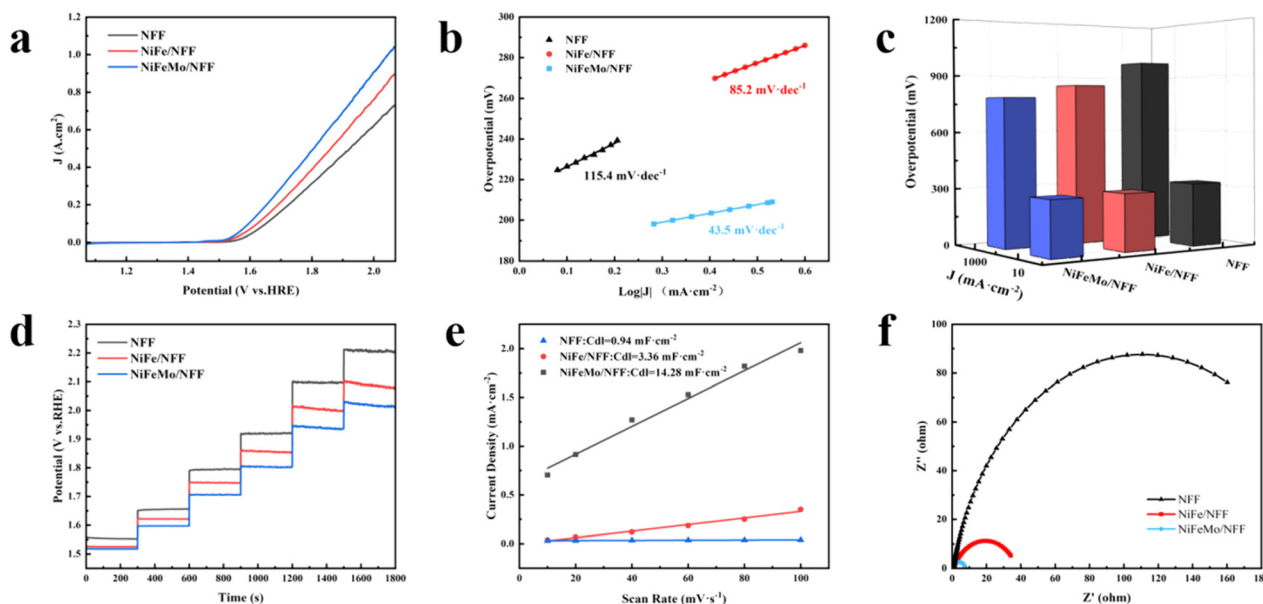

Fig. 5 (a) Linear sweep voltammetry (LSV) curves of NFF, NiFe/NFF, and NiFeMo/NFF. (b) Tafel plots for the oxygen evolution reaction (OER). (c) Overpotential comparison under current densities of 10 mA cm^{-2} and 1000 mA cm^{-2}. (d) ISTEP response curves form 10 mA cm^{-2} to 1000 mA cm^{-2}. (e) C_{dl} capacitance. (f) Nyquist impedance spectra.

ively (Table S3†). These data suggested that NiFeMo/NFF had the largest electrochemical specific surface area and more effective active components on NFF, aligning with the results of SEM characterization. The doping of Mo and Fe led to increased electrochemical active area due to the nanosheet and nanoparticle structures loaded on the surface.

Moreover, the results of the alternating current impedance test showed that the solution resistance R_S was 0.71 Ω, the charge transfer resistance R_{ct} of NFF was 219.7 Ω, and the NiFeMo/NFF composite material doped with iron and molybdenum reduced it to 6.88 Ω, as shown in Table S4.† Post-calcination, NiFeMo/NFF exhibited the lowest R_{ct} compared with that of NiFe/NFF. These findings demonstrated that the introduction of Mo effectively reduced the electron transfer resistance of the catalyst, establishing a more efficient charge transfer pathway. Combined with the results of the Tafel test, NiFeMo/NFF displayed superior intrinsic catalytic activity towards the OER.

3.3 Stability and applications

To systematically evaluate the long-term operational stability of NiFeMo/NFF, NiFe/NFF, and NFF electrodes, we conducted 500 start–stop durability tests combined with cyclic voltammetry (CV) before and after cycling. As shown in Fig. 6a, the LSV curves revealed that NiFeMo/NFF exhibited a significant increase in OER activity with cycling number, while NFF and NiFe/NFF showed distinct behaviors. By extracting current-

density values at 1.87 V (*vs.* RHE) across 1–500 cycles (Fig. 6b), we observed that NFF maintained consistent current density throughout all cycles, indicating no notable structural/chemical evolution. In contrast, NiFe/NFF activated gradually over time, suggesting moderate activation processes. Most notably, NiFeMo/NFF demonstrated a marked increase in current density, underscoring the synergistic effect of electrochemical etching and thermal annealing in dynamically reconstructing active surface boundaries. We conducted SEM characterization specifically on NiFeMo/NFF electrode sheets after prolonged electrolysis (Fig. S5†). The main structure of the catalyst remained intact after 210 h of continuous operation, with no significant particle agglomeration or structural collapse observed. Compared with the initial state, the morphology and distribution density of the nanosheet array remained stable. The selected area electron diffraction patterns indicated that the lattice structure had not undergone significant changes. It showed that the lattice parameters had no obvious change after the reaction, and the performance was stable. The above result highlighted that Mo doping stabilized active sites against degradation, but also enabled continuous regeneration of high-performance catalytic interfaces through iterative electrochemical processing.

We employed a "customized" NiFeMo/NFF composite anode paired with a team-developed Ni-based cathode to construct an alkaline electrolysis system with an effective electrode area of 20 cm². Construction of the electrolytic cell is depicted in
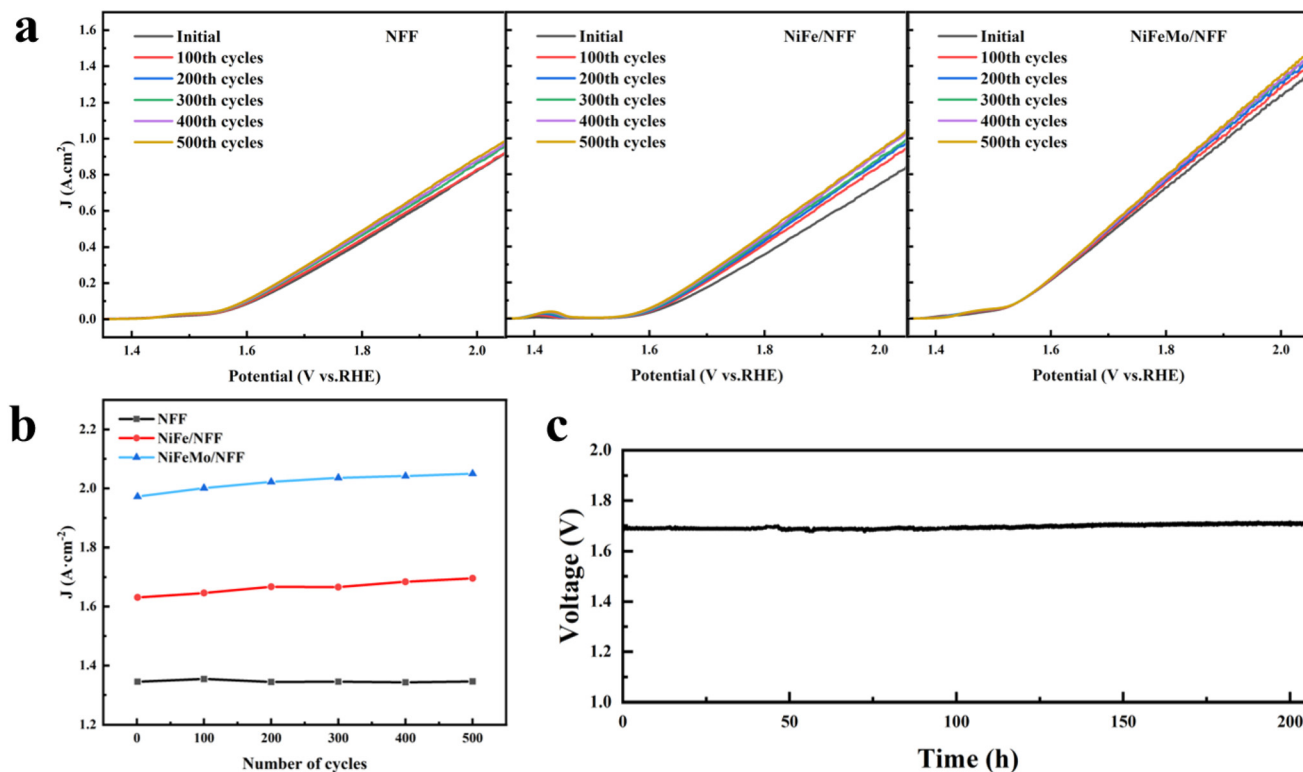

Fig. 6 (a) Linear sweep voltammetry (LSV) curves of NFF, NiFe/NFF, and NiFeMo/NFF under different cycling cycles. (b) Comparative analysis of current density. (c) Long-term stability test of NiFeMo/NFF at 3000 A m^{-2}.
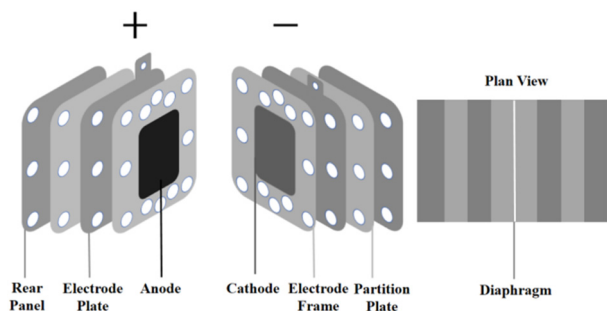
Fig. 7 Structure of the electrolytic cell (schematic).

Fig. 7. Under simulated industrial fluctuating conditions (30 wt% KOH electrolyte, 85 °C operation temperature, and current density of 3000 A m^{-2}), the system underwent continuous electrolysis for 210 h. As shown in Fig. 6c, the voltage–time curve revealed stable operation at 1.695 V with a voltage fluctuation range of ±1.1%, demonstrating exceptional electrochemical stability and activity under harsh operational parameters. Notably, the NiFeMo/NFF anode maintained consistent voltage output even at the industrially relevant current density of 3000 A m^{-2}, confirming its capability to meet the technical requirements of large-scale "green" hydrogen-production systems. This performance highlighted the potential for practical implementation of the material in next-generation electrolyzers.

4 Conclusions

We fabricated a three-dimensional porous nickel–iron-based self-supported electrocatalyst (NiFeMo/NFF) *via* an electrochemical *in situ* etching strategy. The catalyst featured ultrathin nanosheet aggregates and nanoparticles constructed synergistically, demonstrating significantly enhanced OER performance and industrial-level stability. Electrochemical measurements revealed that NiFeMo/NFF achieved overpotentials of 288 mV at 10 mA cm^{-2} and 784 mV at 1000 mA cm^{-2} in alkaline electrolytes. Under simulated industrial electrolysis conditions (30% KOH electrolyte, 85 °C, current density of 3000 A m^{-2}), the electrode exhibited exceptional operational stability, maintaining a stable output voltage of 1.695 V for 210 h with a negligible voltage decay rate of 100 μV h^{-1}, highlighting its robust adaptability to harsh operational environments. After systematic comparison of the electrochemical data of several advanced OER catalysts in recent literature (Table S5†), our prepared NiFeMo/NFF was in a relatively leading position in the active-stability synergistic index.

Furthermore, we elucidated the dynamic evolution mechanisms of transition metal catalysts under industrially relevant current densities through coordinated elemental doping and structural engineering. These findings provide theoretical insights and practical hints for designing highly active and durable non-precious metal electrodes for large-scale green hydrogen production.

Author contributions

Zhiqun Bai conceived the idea of the project and supervised the project. Ruoxuan Guo synthesized and characterized NiFeMo/NFF, and analyzed electrochemical data. Jingwang Kuang analyzed partial electrochemical data and co-authored the manuscript with Zhiqun Bai. Jingchao Liu and Yang Tang coordinated manuscript submission and journal communication. Huifang Chen, WeiHao Sha, Ao Xie and Pingyu Wan discussed the results and commented on the manuscript.

Conflicts of interest

There are no conflicts of interest to declare.

Data availability

The data supporting this article have been included as part of the ESI† and are available from the corresponding author upon reasonable request.

Acknowledgements

References

1 P. J. Megía, A. J. Vizcaíno, J. A. Calles and A. Carrero, Hydrogen production technologies: From fossil fuels toward renewable sources. A mini review, *Energy Fuels*, 2021, **35**(20), 16403–16415.

2 K. G. Dos Santos, C. T. Eckert, E. De Rossi, *et al.*, Hydrogen production in the electrolysis of water in brazil, a review, *Renewable Sustainable Energy Rev.*, 2017, **68**, 563–571.

3 X. Liu, J. Chi, B. Dong, *et al.*, Recent progress in decoupled H$_2$ and O$_2$ production from electrolytic water splitting, *ChemElectroChem*, 2019, **6**(8), 2157–2166.

4 Z. Yu, Y. Duan, X. Feng, *et al.*, Clean and Affordable Hydrogen Fuel from Alkaline Water Splitting: Past, Recent Progress, and Future Prospects, *Adv. Mater.*, 2021, **33**, e2007100.

5 D. Bogdanov, M. Ram, A. Aghahosseini, *et al.*, Low-cost renewable electricity as the key driver of the global energy transition towards sustainability, *Energy*, 2021, **227**, 120467.

6 Z. Lu, W. Xu, Z. Wei, *et al.*, Three-dimensional NiFe layered double hydroxide film for high-efficiency oxygen evolution reaction, *Chem. Commun.*, 2014, **50**(49), 6479–6482.

7 D. Lei, L. Kui, X. Zhiqiang, *et al.*, Constructing Ultrathin W-Doped NiFe Nanosheets via Facile Electrosynthesis as Bifunctional Electrocatalysts for Efficient Water Splitting, *ACS Appl. Mater. Interfaces*, 2021, **13**(17), 20070–20080.

8   Z. Chen, Z. Li, M. Zhang, *et al.*, Preparation of Non-Noble Metal Catalyst $FeCo_2O_4/MoS_2$ for Production of Hydrogen and Oxygen by Electrochemical Decomposition of Water, *Inorganics*, 2024, **12**(8), 229–229.

9   D. Chen, Z. Chen, X. Zhang, *et al.*, Exploring single atom catalysts of transition-metal doped phosphorus carbide monolayer for HER:A first-principles study, *Energy Chem.*, 2021, **35**, 155–162.

10 C. Xie, W. Chen, Y. Wang, *et al.*, Dynamic evolution processes in electrocatalysis: structure evolution, characterization and regulation, *Chem. Soc. Rev.*, 2024, **22**, 10852–10877.

11 W. Feng, B. Chang, Y. Ren, *et al.*, Proton Exchange Membrane Water Splitting: Advances in Electrode Structure and Mass-Charge Transport Optimization, *Adv. Mater.*, 2025, e2416012.

12 T. Wang, B. Li, P. Wang, *et al.*, Modulation of electronic structure of Ni_3S_2 via Fe and Mo co-doping to enhance the bifunctional electrocatalytic activities for HER and OER, *J. Colloid Interface Sci.*, 2024, 672715–672723.

13 A. D. Kuznetsov, B. Han, Y. Yu, *et al.*, Tuning Redox Transitions via Inductive Effect in Metal Oxides and Complexes, and Implications in Oxygen Electrocatalysis, *Joule*, 2018, **2**(2), 225–244.